Lifshitz transition enhanced triplet p_z-wave superconductivity in hydrogen-doped KCr_3As_3

Ming Zhang,[1,*] Juan-Juan Hao,[1,*] Xianxin Wu,[2,3,†] and Fan Yang[1,‡]
[1]*School of Physics, Beijing Institute of Technology, Beijing 100081, China*
[2]*Max-Planck-Institut für Festkörperforschung, Heisenbergstrasse 1, D-70569 Stuttgart, Germany*
[3]*CAS Key Laboratory of Theoretical Physics, Institute of Theoretical Physics, Chinese Academy of Sciences, Beijing 100190, China*

(Received 4 December 2021; revised 23 March 2022; accepted 23 March 2022; published 13 April 2022)

The recently synthesized air-insensitive hydrogen-doped KCr_3As_3 superconductor has aroused great research interest. This material has, for the first time in the research area of the quasi-one-dimensional (quasi-1D) Cr-based superconductivity (SC), realized a tunability through charge doping, which will potentially significantly push the development of this area. Here, based on the band structure from first-principles calculations, we construct a six-band tight-binding model equipped with multiorbital Hubbard interactions and adopt the random-phase-approximation approach to study the hydrogen-doping dependence of the pairing symmetry and superconducting T_c. Under the rigid-band approximation, our pairing phase diagram is occupied by the triplet p_z-wave pairing throughout the hydrogen-doping regime $x \in (0.4, 1)$ in which SC has been experimentally detected. Remarkably, the x dependence of T_c shows a peak at the three-dimensional–quasi-1D Lifshitz transition point, although the total density of states exhibits a dip there. The corresponding doping level is near the experimental estimation of the optimal doping level. A thorough investigation of the band structure reveals type-II van Hove singularities (VHSs) in the γ band, which favor the formation of the triplet SC. It turns out that the γ Fermi surface (FS) comprises two flat quasi-1D FS sheets almost parallel to the $k_z = 0$ plane and six almost perpendicular tubelike FS sheets, and the type-II VHS just lies in the boundary between these two FS parts. Furthermore, the $|k_z|$ of the van Hove planes reaches the maximum near the Lifshitz-transition point, which pushes the T_c of the p_z-wave SC to the maximum. Our results appeal for more experimental access into this intriguing superconductor.

DOI: 10.1103/PhysRevB.105.134509

I. INTRODUCTION

In recent years, the quasi-one-dimensional (1D) superconductor family $A_2M_3As_3$ (A = Na, K, Rb, and Cs; M = Cr and Mo) [1–18] with highest superconducting T_c above 10 K [17] has attracted tremendous research interest. These compounds consist of alkali-metal-atom-separated $[(M_3As_3)^{2-}]_\infty$ double-walled subnanotubes with the low-energy degrees of freedom dominated by the M 3d orbitals [19,20], which are proposed to be strongly correlated [5,8,14,21–26], implying an electron-interaction-driven pairing mechanism. Various experiments [1–6,8,9,12,13,18] have revealed the unconventional pairing feature of this superconductor family, with evidence suggesting the existence of line gap nodes [2,4] and possible spin triplet pairing states [1–3,8,12,18,27,28]. This family, however, has a serious drawback in that these materials are unstable in the atmosphere, which hinders widespread experimental studies on them. Furthermore, the lack of tunability through charge doping, another shortcoming, prevents the understanding of the nature of the electron correlations.

Slightly after the synthesization of the $A_2Cr_3As_3$ (233) family, its air-insensitive cousin family $A_1Cr_3As_3$ (133) was obtained by removing half of the A^+ ions through an ethanol bath at room temperature [29–32]. The 133 family shares similar quasi-one-dimensional (quasi-1D) crystalline structure and low-energy degrees of freedom with the 233 family [33]. Initially, there exists obvious conflict on the ground-state property of the 133 family. While the works reported in Refs. [29,30,34] suggest the 133 family to be nonsuperconducting with a spin-glass ground state, definite evidence for superconductivity (SC) has been identified in the work reported in Refs. [31,32]. This conflict was finally reconciled by the revelation using neutron and x-ray diffraction [35] that the hydrogen atoms intercalated in the material play the crucial role for the appearance of SC [35–37]. The difference between nonsuperconducting and superconducting $A_1Cr_3As_3$ samples mainly lies in the hydrogen concentration; i.e., the stoichiometric formula of both samples should be $A_1H_xCr_3As_3$ but their x are different. The density functional theory (DFT)-based first-principles calculations suggest that the main role of the doped hydrogen atoms is to donate electrons [35,38], whose concentration is now experimentally tunable [35–37]. Therefore, the hydrogen concentration x in the 133 family provides an effective way, i.e., charge doping, to tune the correlated quantum states. For example, while the samples with $x < 0.35$ are found to be nonsuperconducting with a spin-glass ground state, SC emerges in the samples with higher x, with the optimal x for SC roughly estimated to be within the range $x \in (0.65, 0.71)$ [35].

The DFT-based calculations [35] show that the chemical reaction between KCr_3As_3 and H_2 will form $KHCr_3As_3$ with

---

[*] These authors contributed equally to this work.

[†] xianxinwu@gmail.com

[‡] yangfan_blg@bit.edu.cn

similar quasi-1D structure as that of KCr_3As_3, but with the hydrogen atoms intercalated at the center of Cr octahedra in the $[(wCr_3As_3)^{2-}]_\infty$ subnanotubes. No unstable phonon modes are found for this structure, suggesting its stability [35]. In the aspect of band structure [35,38], the role of the intercalated hydrogen atoms mainly lies in the rise of the Fermi energy E_F, besides modest distortions to the bands near E_F. Therefore, we can say that in $KHCr_3As_3$, H has metallic bonding and acts as an electron donor. Furthermore, the H concentration x in the material is experimentally tunable [35,38]. While the DFT results for $x = 0$ yield an interlayer-antiferromagnetic ordered ground state [33], those for $x = 1$ suggest a nonmagnetic ground state with short-ranged ferromagnetic [38] or antiferromagnetic [35] spin fluctuations, which might mediate SC. Therefore, the phase diagram in $KH_xCr_3As_3$ via tuning x is like those of the cuprates and the iron pnictide superconductors wherein magnetic order states are usually found to be proximate to the SC, suggesting the relevance of the e-e interaction-driven pairing mechanism. However, detailed theoretical studies about these phase diagrams are still missing.

A prominent feature of the band structure of $KH_xCr_3As_3$ lies in the presence of a Lifshitz transition at about $x = 0.75$ [38]. From the DFT calculations, the low-energy degrees of freedom near E_F for the $KH_xCr_3As_3$ include the Cr $3d_{xy}$, $3d_{x^2-y^2}$, and $3d_{z^2}$ orbitals. At $x = 1$, there are three bands which cross the Fermi surface (FS), including the quasi-1D α and β bands and the three-dimensional (3D) γ band. When the H concentration x decreases to about $x = 0.75$, the γ band experiences a Lifshitz FS-topology transition, during which its 3D FSs are changed to two disconnected quasi-1D FS sheets (see Fig. 3 of Ref. [38]). The physical consequences of this Lifshitz transition, however, have not been thoroughly investigated.

In this article, we study the pairing symmetry of $KH_xCr_3As_3$ via the random-phase-approximation (RPA) approach [39–47], adopting the tight-binding (TB) model constructed from fitting our DFT band structure. Adopting the band structure for $x = 1$, we use the rigid-band approximation to study the x dependence of the pairing symmetry and the superconducting T_c in the regime $x \in (0.4, 1)$ wherein definite evidence of SC is experimentally detected [35]. Our results yield that the triplet p_z-wave pairing is the leading pairing symmetry in this doping regime. Particularly, the highest T_c is obtained at the Lifshitz-transition doping level. A careful investigation of the band structure suggests that the presence of the type-II van Hove singularities (VHSs) [48–52] on the FSs are responsible for the triplet pairing, and the Lifshitz transition further favors the p_z-wave pairing symmetry. Our results appeal for more experimental access into this intriguing superconductor hosting possible triplet p_z-wave topological SC.

The rest of this paper is organized as follows: In Sec. II, we provide our results from first-principles calculations based on DFT for the band structure of $KHCr_3As_3$, after which we construct its effective TB model. In Sec. III, we study the pairing symmetry of the system via the RPA approach, and present the pairing phase diagram. In Sec. IV, we focus on the analysis of the band structure to reveal the role of the Lifshitz transition and the type-II VHSs on the γ FS, which favors the triplet p_z-wave SC. Our results are summarized in Sec. V together with some discussions about possible experimental implications.

II. BAND STRUCTURE AND THE TB MODEL

A. The DFT band structure

As shown in Fig. 1(a), the crystal structure of $KHCr_3As_3$ is quasi 1D, and the basic unit is an infinite linear chain double-walled subnanotube (DWSN) $[(Cr_3As_3)^{2-}]_\infty$, and these are connected to each other through K^+ alkaline cations [35]. Cr atoms should be covalently bonded with As atoms, and As atoms should be bonded with K^+ ions to separate the positively charged Cr and K atoms. They are composed of Cr_6 (or As_6) octahedrons on the shared surface along the crystallographic c direction and the H atom is located in the center of these octahedrons. $KHCr_3As_3$ can be viewed as H-doped KCr_3As_3 with the doping level $x = 1$. Similar to KCr_3As_3, $KHCr_3As_3$ has a centrosymmetric structure, with space group $P6_3/m$ (No. 176, point group C_{6h}), in which Cr and As atoms form double-walled subnanotubes along the c axis.

The band structure of the $KHCr_3As_3$ material was calculated using the method of first-principles DFT theory as implemented in the QUANTUM ESPRESSO (QE) code [53]. The cutoff energy for expanding the wave functions into a plane-wave basis was set to 60 Ry and the adopted k-point grid is 5×5×11. The exchange-correlation energy was described by the generalized gradient approximation (GGA) using the Perdew-Burke-Ernzerhof (PBE) functional [54]. The lattice parameters from relaxation are $a = 9.09481$ Å and $c = 4.17703$ Å, which are consistent with the experimental data in Ref. [35]. To obtain the six-band low-energy model, we initialize d_{z^2} and d_{xy/x^2-y^2} orbitals at the centers of Cr triangles and then perform the calculations of maximal localization for these orbitals using WANNIER90 [55].

Our band structure calculated from the DFT calculations is shown in Fig. 1(b) along the lines connecting the high-symmetry points marked in the Brillouin zone (BZ) shown in Fig. 1(c). It can be seen that there are five bands near the Fermi level (marked as α, β, γ, δ, and ϵ), among which only the three ones α, β, and γ cross the FS, which are mainly composed of $3d_{z^2}$, $3d_{x^2-y^2}$, and $3d_{xy}$ orbitals of Cr atoms. In comparison with the nonmagnetic band structure of KCr_3As_3 [33,47], our present one for $KHCr_3As_3$ shows a similar shape, with only modest distortion near the Fermi level that is relatively increased by about 0.14 eV. Therefore, the inserted hydrogen atoms in $KHCr_3As_3$ can be well viewed as effective electron donors, consistent with previous results [35,38]. The FSs of the system are shown in Fig. 1(c), which includes two quasi-1D FSs, α and β, and one 3D FS, γ. While the α and β FSs each contain two disconnected FS sheets nearly parallel with the xy plane, the γ FS only contains one globally connected sheet.

When the interaction in the partially filled d orbital is strong, an additional on-site interaction should be added in the calculations (GGA + U calculations) in order to get more accurate electronic structure. From available experimental evidence for $KH_xCr_3As_3$, however, no strongly correlated state is clearly identified and thus the interaction is expected to not be that strong. However, in checking the robustness of

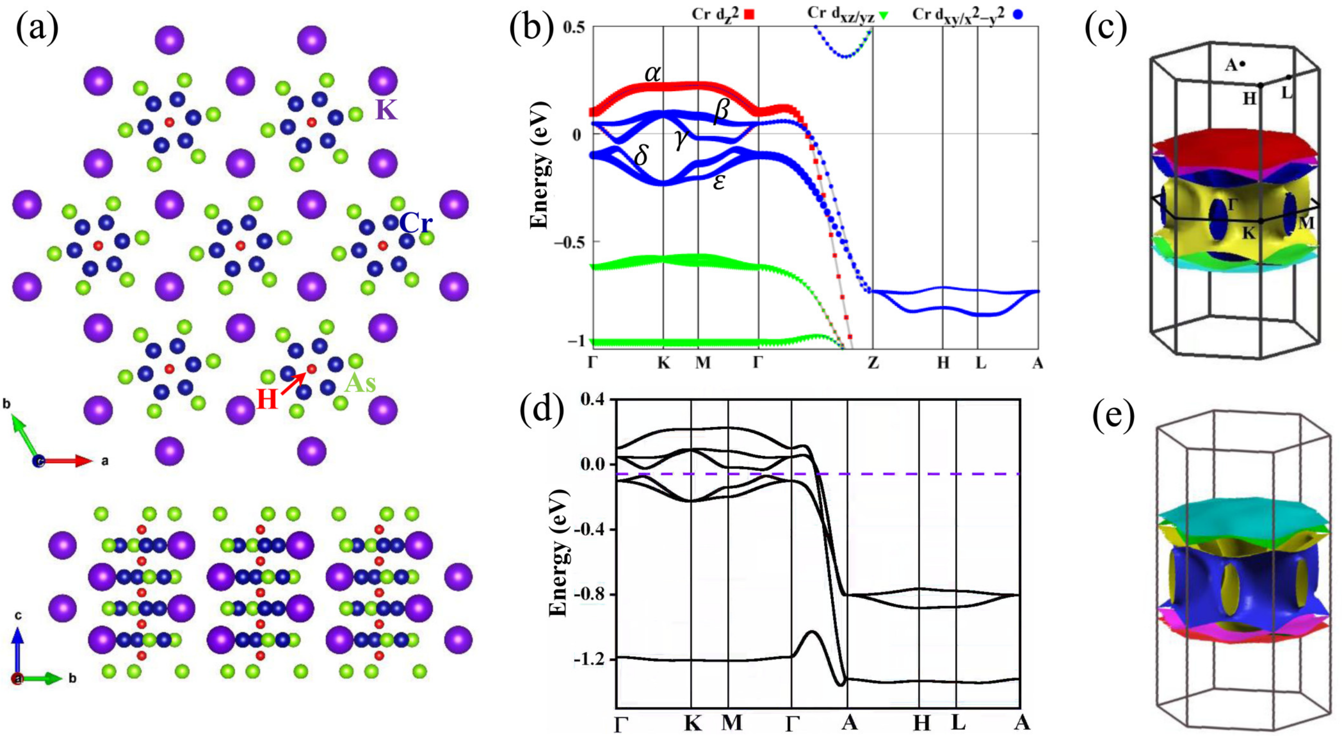

FIG. 1. (a) The top and side views for the crystal structure of $KHCr_3As_3$. (b) Band structure of $KHCr_3As_3$ along the high-symmetry lines, with the red square, green triangle, and blue circle being drawn proportional to the weight of Cr $3d_{z^2}$, $3d_{xy}$, and $3d_{x^2-y^2}$, respectively. The five bands around the Fermi level are marked as α through ε, respectively. (c) FSs of $KHCr_3As_3$ from DFT calculations, with the high-symmetry points and the band indices for the three FSs marked. (d) Band structures and (e) FSs from the six-band TB model. Hydrogen doping at the purple dashed line in (d) is 0.6.

the electronic structure, we performed GGA + U calculations with $U = 2.3$ eV and $J = 0.96$ eV (parameters from Ref. [56]) and the obtained band structure is displayed in Fig. 2, in comparison with normal GGA calculations. We find that the band structure from GGA + U calculations just changes slightly near the Fermi level and exhibits more noticeable change away from the Fermi level. Therefore, the change of band structure at low energy is very small when including additional interactions.

In this paper, we neglect the spin-orbit coupling (SOC), as the atoms are not heavy in $KHCr_3As_3$. Including the SOC will introduce some gap opening around the Γ and K points [57]. However, the relatively weak SOC will not change the band structure that much and thus will not change the pairing symmetry. Therefore, we focus on the band structure without SOC here.

B. The TB model

As the bands near the Fermi level are predominantly contributed by Cr d_{z^2}, d_{xy}, and $d_{x^2-y^2}$ orbitals, we construct a six-band TB model to capture the low-energy bands in the DFT calculations, where A_{1g} and E_{2g} orbitals are located at the centers of two Cr triangles. This effective model is analogous to that of $K_2Cr_3As_3$ but with the higher-symmetry point group C_{6h} [21]. To obtain the effective hopping parameters directly from DFT calculations, we initialize d_{z^2} (A_{1g}) and d_{xy/x^2-y^2} (E_{2g}) orbitals at the centers of Cr triangles [(0,0,0/0.5)] and then perform the calculations of maximal localization for these orbitals using WANNIER90 [55]. As the crystal symmetry is slightly broken in the resulting model, we further performed symmetrization on the obtained hopping parameters in real

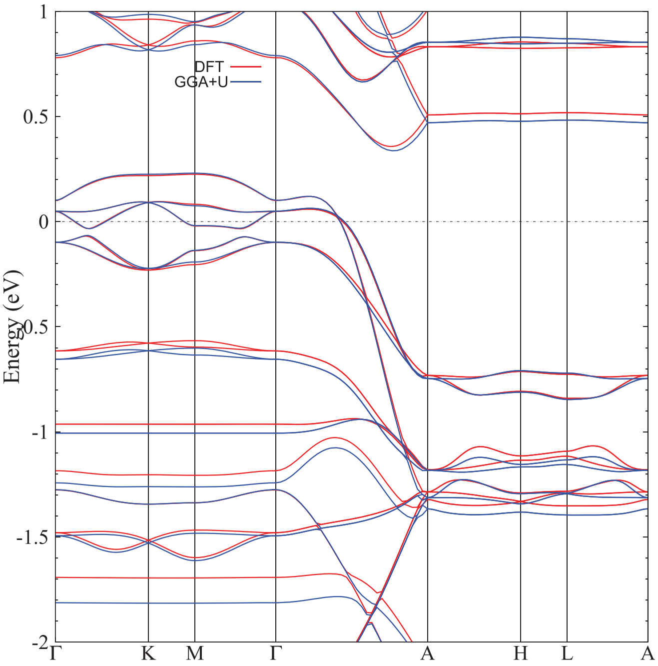

FIG. 2. Band structures of $KH_xCr_3As_3$ with GGA (red lines) and GGA + U (blue lines, $U = 2.3$ eV and $J = 0.96$ eV).

space using symmetry operations in C_{6h}. The obtained TB Hamiltonian in momentum space can be expressed as

$$H_{\text{TB}} = \sum_{\boldsymbol{k}\mu\nu\sigma} h_{\mu\nu}(\boldsymbol{k}) c^{\dagger}_{\mu\sigma}(\boldsymbol{k}) c_{\nu\sigma}(\boldsymbol{k}), \tag{1}$$

where $\mu, \nu = 1, \ldots, 6$ indicate the orbital-sublattice indices, containing the d_{z^2}, $d_{x^2-y^2}$, and d_{xy} orbitals of sublattice A and sublattice B. The elements of the $h(\boldsymbol{k})$ matrix are

$$h_{\mu\nu}(\boldsymbol{k}) = \sum_{r_1,r_2,r_3} t_{\mu\nu}^{r_1,r_2,r_3} e^{i\boldsymbol{k}\cdot(r_1\boldsymbol{a_1}+r_2\boldsymbol{a_2}+r_3\boldsymbol{a_3})}, \tag{2}$$

with $\boldsymbol{a_1} = (\frac{\sqrt{3}}{2}a_0, -\frac{1}{2}a_0, 0)$, $\boldsymbol{a_2} = (0, a_0, 0)$, and $\boldsymbol{a_3} = (0, 0, c_0)$. The data of $t_{\mu\nu}^{r_1,r_2,r_3}$ for $r_1 \in [-4, 4]$, $r_2 \in [-2, 2]$, $r_3 \in [-6, 6]$, and $\mu, \nu \in [1, 6]$ are provided in the Supplemental Material (SM) [58]. Note that in the absence of SOC and magnetic order, the time-reversal symmetry requires these hopping parameters to be real. The band structure from this model is shown in Fig. 1(d), which is in good agreement with that of the DFT [Fig. 1(b)] near the Fermi level.

Although the above-provided band structure and TB model only accurately adapt to KHCr$_3$As$_3$, we take the rigid-band approximation and adopt them to describe the band structure of KH$_x$Cr$_3$As$_3$ with only the chemical potential tuned according to the variation of x. Note that each unit cell contains two H atoms and each H donates one electron. The validity of this approximation is based on the similarity between the band structures of KHCr$_3$As$_3$ ($x = 1$) and KCr$_3$As$_3$ ($x = 0$) [35]. However, since the two band structures are not exactly the same, we limit our study to the regime not too far from $x = 1$, where the rigid-band approximation adapts better. In our calculations, we set x to be within the doping regime $x \in (0.4, 1)$, in which definite evidence of SC has been detected [35,38].

III. THE RPA-BASED PAIRING PHASE DIAGRAM

We adopt the following extended Hubbard model Hamiltonian in our study:

$$\begin{aligned} H &= H_{\text{TB}} + H_{\text{int}}, \\ H_{\text{int}} &= U \sum_{i\mu} n_{i\mu\uparrow} n_{i\mu\downarrow} + V \sum_{i,\mu<\nu} n_{i\mu} n_{i\nu} + J_H \sum_{i,\mu<\nu} \left[\sum_{\sigma\sigma'} c^{+}_{i\mu\sigma} c^{+}_{i\nu\sigma'} c_{i\mu\sigma'} c_{i\nu\sigma} + (c^{+}_{i\mu\uparrow} c^{+}_{i\mu\downarrow} c_{i\nu\downarrow} c_{i\nu\uparrow} + \text{H.c.}) \right]. \end{aligned} \tag{3}$$

Here, $n_{i\mu} = n_{i\mu\uparrow} + n_{i\mu\downarrow}$ denotes the number of electrons in orbital μ at lattice site i. $c^{+}_{i\mu\sigma}$ ($c_{i\mu\sigma}$) is the electron creation (annihilation) operator at lattice site i with orbital μ and spin σ. The interaction parameters U, V, and J_H denote the intraorbital and interorbital Hubbard repulsion, and the Hund's rule coupling (as well as the pair hopping), respectively, which satisfy the relation $U = V + 2J_H$.

A. Bare susceptibility

We first define the following bare susceptibility tensor in the normal state for the noninteracting case:

$$\begin{aligned} \chi^{(0)}_{pqst}(\boldsymbol{k}, \tau) \equiv \frac{1}{N} \sum_{\boldsymbol{k}_1\boldsymbol{k}_2} &\langle T_\tau c^{\dagger}_p(\boldsymbol{k}_1, \tau) c_q(\boldsymbol{k}_1 + \boldsymbol{k}, \tau) \\ &\times c^{\dagger}_s(\boldsymbol{k}_2 + \boldsymbol{k}, 0) c_t(\boldsymbol{k}_2, 0)\rangle_0. \end{aligned} \tag{4}$$

Here $\langle\cdots\rangle_0$ denotes the thermal average for the noninteracting system, T_τ denotes the imaginary time-ordered product, and the tensor indices $p, q, s, t = 1, \ldots, 6$ denote the orbital-sublattice indices. Fourier transformed to the imaginary frequency space, the bare susceptibility can be expressed by the following explicit formulism:

$$\begin{aligned} \chi^{(0)}_{pqst}(\boldsymbol{k}, i\omega_n) =& \frac{1}{N} \sum_{\boldsymbol{k}'\alpha\beta} \xi^{\alpha}_t(\boldsymbol{k}') \xi^{\alpha*}_p(\boldsymbol{k}') \xi^{\beta}_q(\boldsymbol{k}' + \boldsymbol{k}) \\ &\times \xi^{\beta*}_s(\boldsymbol{k}' + \boldsymbol{k}) \frac{n_F(\varepsilon^{\beta}_{\boldsymbol{k}'+\boldsymbol{k}}) - n_F(\varepsilon^{\alpha}_{\boldsymbol{k}'})}{i\omega_n + \varepsilon^{\alpha}_{\boldsymbol{k}'} - \varepsilon^{\beta}_{\boldsymbol{k}'+\boldsymbol{k}}}, \end{aligned} \tag{5}$$

where $\alpha, \beta = 1, \ldots, 6$ are band indices, $\varepsilon^{\alpha}_{\boldsymbol{k}}$ and $\xi^{\alpha}(\boldsymbol{k})$ are the αth eigenvalue (relative to the chemical potential μ_c) and eigenvector of the TB model, respectively, and n_F is the Fermi-Dirac distribution function.

The susceptibility tensor $\chi^{(0)}_{pqst}(\boldsymbol{k}, i\omega)$ defined in the above can be viewed as a matrix $\chi^{(0)pq}_{st}(\boldsymbol{k}, i\omega)$ by taking the combined pq indices as the row index and the combined st indices as the column index. In Fig. 3, we show the $\boldsymbol{k}$ dependence of the largest eigenvalue $\chi(\boldsymbol{k})$ of the zero-frequency susceptibility matrix $\chi^{(0)pq}_{st}(\boldsymbol{k}, i\omega_n = 0)$ for three different doping levels, i.e., $x = 1$ [Figs. 3(a)–3(c)], $x = 0.6$ [Figs. 3(d)–3(f)], and $x = 0.4$ [Figs. 3(g)–3(i)]. Figures 3(a), 3(d), and 3(g) in the first row are along the high-symmetry lines in the BZ; Figs. 3(b), 3(e), and 3(h) in the second row are on the $k_z = 0$ plane; and Figs. 3(c), 3(f), and 3(i) in the third row are on the $k_z = \pi$ plane. Note that here $x = 1$ denotes KHCr$_3$As$_3$, $x = 0.4$ is the lowest electron-doping level we consider, and the doping level $x = x_c = 0.6$ indicates the Lifshitz-transition point in our TB model. This doping level is slightly lower than the $x_c = 0.73$ in our DFT band structure obtained via the QE code and the $x_c = 0.75$ in previous DFT band structure obtained via the VASP code [38], mainly due to the slight deviation between our TB model and the DFT band structures.

Figure 3 illustrates two doping-dependent features for the distributions of the susceptibilities in the BZ. The first feature lies in that the spin correlations are globally enhanced when the electron-doping level is decreased from $x = 1$ (for KHCr$_3$As$_3$) to $x = 0$ (for KCr$_3$As$_3$). For example, let us focus on the doping dependence of the maximum value of $\chi(\boldsymbol{k})$ throughout the BZ, i.e., the peak value χ_{Max} at the momentum k_0 for a fixed doping level x. For $x = 1$, χ_{Max} is about 2.9 and the corresponding k_0 is within the $k_z = 0$ plane, as shown in Fig. 3(b); for $x = 0.6$, χ_{Max} is about 3.6 around the Γ point, as

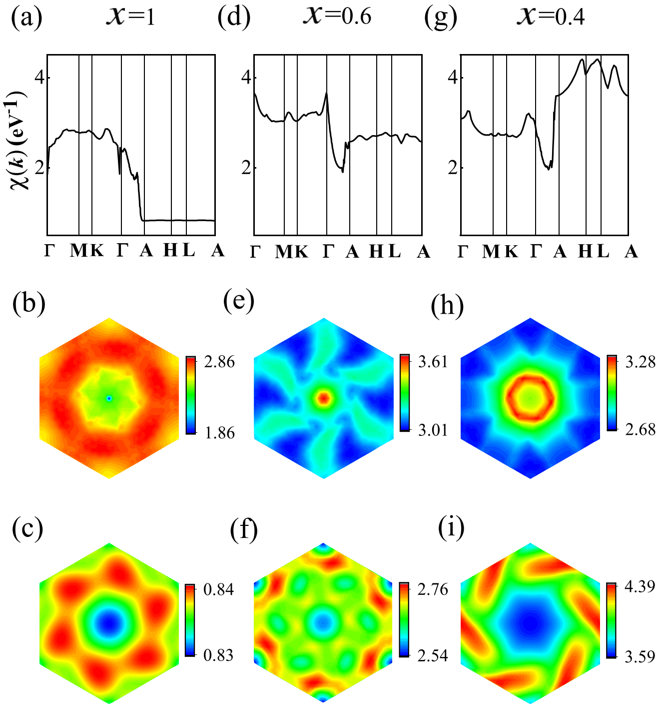

FIG. 3. The $\boldsymbol{k}$-space distribution of the largest eigenvalue $\chi(\boldsymbol{k})$ of the susceptibility matrix $\chi^{(0)pq}_{st}(\boldsymbol{k}, i\omega_n = 0)$ for (a–c) KCr$_3$As$_3$H, (d–f) KCr$_3$As$_3$H$_{0.6}$, and (g–i) KCr$_3$As$_3$H$_{0.4}$. From top to bottom are the largest eigenvalues of the susceptibility matrix $\chi^{(0)}_{pqst}(\boldsymbol{k}, i\omega_n = 0)$ along the high-symmetry lines in the Brillouin zone, on the $k_z = 0$ plane, and on the $k_z = \pi$ plane, respectively.

shown in Fig. 3(e); while for $x = 0.4$, χ_{Max} is further enhanced to 4.4 and the corresponding k_0 moves to the $k_z = \pi$ plane, as shown in Fig. 3(i). This feature suggests that the tendency toward magnetic order increases from KHCr$_3$As$_3$ to KCr$_3$As$_3$, which is consistent with the experiments [34,35] and previous DFT results [33,38]. The second feature lies in the momentum $\boldsymbol{k}_0$ where the susceptibility peak gradually shifts from within the $k_z = 0$ plane to within the $k_z = \pi$ plane, reflecting the variation from interlayer ferromagnetic correlations for KHCr$_3$As$_3$ to interlayer antiferromagnetic correlations for KCr$_3$As$_3$, also consistent with previous DFT calculations [33,38].

Although the spin fluctuations in both the $x = 1$ and $x = 0.6$ cases are interlayer ferromagnetic, there is obvious difference between them in the aspect of the intralayer pattern. Figure 3(a) and 3(b) show that the susceptibility for $x = 1$ is smooth in the $k_z = 0$ plane without obvious peaks. Therefore, the intralayer spin fluctuation pattern for this doping level is neither typical ferromagnetic nor typical antiferromagnetic, but rather their competition, consistent with Ref. [35]. The situation changes for the Lifshitz-transition doping $x = 0.6$, for which Figs. 3(d) and 3(e) show that the susceptibility sharply peaks at the Γ point, implying typical ferromagnetic spin fluctuations. In Fig. 5(a), the doping dependence of the susceptibility for the Γ point is shown, which exhibits a peak near $x = 0.6$, suggesting that the ferromagnetic spin fluctuations are strongest near the Lifshitz transition. Such typical ferromagnetic fluctuations can favor the formation of spin-triplet SC, as will be shown in the following.

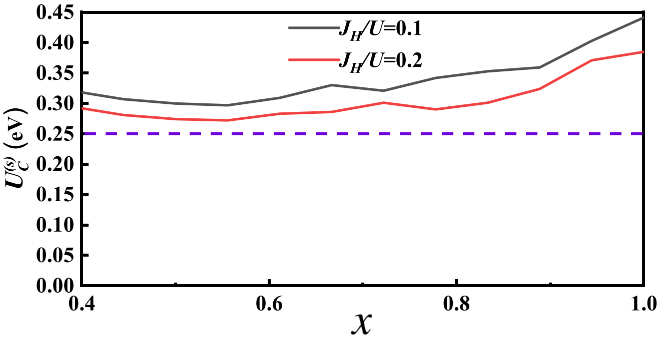

FIG. 4. Critical interaction U_c of the RPA spin susceptibility as a function of hole doping. The red and gray lines are for $J_H = 0.2U$ and $J_H = 0.1U$, respectively. In the main text, we adopt $U = 0.25$ eV to calculate the pairing strength, in order to avoid magnetic instability.

B. The RPA approach

We further calculate the spin (s) and charge (c) susceptibilities following the standard multiorbital RPA approach [39–47] (see also the Appendix). At the RPA level, the renormalized spin and charge susceptibilities of the system read

$$\chi^{(s,c)}(\boldsymbol{k}, i\omega_n) = [I \mp \chi^{(0)}(\boldsymbol{k}, i\omega_n)U^{(s,c)}]^{-1}\chi^{(0)}(\boldsymbol{k}, i\omega_n). \tag{6}$$

Here the nonzero elements $U^{(s,c)\mu\nu}_{\theta\xi}$ of $U^{(s,c)}$ satisfy $\mu, \nu, \theta, \xi \leqslant 3$ or >3 simultaneously, which are as follows:

$$U^{(s(c))\mu\nu}_{\theta\xi} = \begin{cases} U(U), & \mu = \nu = \theta = \xi \\ J_H(2V - J_H), & \mu = \nu \neq \theta = \xi \\ J_H(J_H), & \mu = \theta \neq \nu = \xi \\ V(2J_H - V), & \mu = \xi \neq \theta = \nu. \end{cases} \tag{7}$$

In Eq. (6), $\chi^{(s,c,0)}(\boldsymbol{k}, i\omega_n)$ and $U^{(s,c)}$ are operated as $6^2 \times 6^2$ matrices (see, for example, Ref. [43]).

Our numerical results suggest that the repulsive Hubbard interactions suppress the charge susceptibility but enhance the spin susceptibility, consistent with previous results [39–46,59–62]. There is a critical interaction strength U_c, where the spin susceptibility diverges, implying the formation of a spin density wave (SDW). The doping dependencies of U_c for $J_H = 0.1U$ and $J_H = 0.2U$ are shown in Fig. 4. At $U < U_c$, Cooper pairing may develop through exchanging spin and/or charge fluctuations. In particular, we consider Cooper pair scatterings both within and between the bands; hence both intra- and interband effective interactions $V^{\alpha\beta}(\mathbf{k}, \mathbf{k}')$ [21] (here $\alpha/\beta = 1, \dots, 6$ are band indices) are accounted for. From the effective interaction vertex $V^{\alpha\beta}(\mathbf{k}, \mathbf{k}')$, we obtain the following linearized gap equation near the superconducting T_c:

$$-\frac{1}{(2\pi)^3}\sum_{\beta} {}_{FS} d^2\boldsymbol{k}'_{\parallel}\frac{V^{\alpha\beta}(\boldsymbol{k}, \boldsymbol{k}')}{v^{\beta}_F(\boldsymbol{k}')}\Delta_\beta(\boldsymbol{k}') = \lambda\Delta_\alpha(\boldsymbol{k}). \tag{8}$$

Here the integration runs along the β FS, the Fermi velocity $v^{\beta}_F(\boldsymbol{k}')$ is the amplitude of the gradient of the band energy at the momentum $\boldsymbol{k}'$, and $\boldsymbol{k}'_{\parallel}$ is the projection of $\boldsymbol{k}'$ on the FS. Superconducting pairing in various channels emerges as the eigenstates of the above gap equation. The leading

TABLE I. The 12 possible pairing symmetries for KCr_3As_3H in the absence of SOC, among which 6 are spin singlet while the rest are spin triplet.

Singlet	Triplet
s	p_z
$(d_{x^2-y^2}, d_{xy})$	$(d_{x^2-y^2}, d_{xy}) \cdot p_z$
$(p_x, p_y) \cdot p_z$	(p_x, p_y)
$f_{x^3-3xy^2} \cdot p_z$	$f_{x^3-3xy^2}$
$f'_{y^3-3x^2y} \cdot p_z$	$f'_{y^3-3x^2y}$
$f_{x^3-3xy^2} \cdot f'_{y^3-3x^2y}$	$f_{x^3-3xy^2} \cdot f'_{y^3-3x^2y} \cdot p_z$

pairing $\Delta_\alpha(\boldsymbol{k})$ is given by the eigenstate corresponding to the largest eigenvalue λ. The critical temperature T_c is related to λ through $T_c \propto e^{-1/\lambda}$.

The eigenvector(s) $\Delta_\alpha(\boldsymbol{k})$ for each eigenvalue λ obtained from gap equation (8) as the basis function(s) forms an irreducible representation of the C_{6h} point group. In the absence of SOC, 12 possible pairing symmetries are possible candidates for the system, which include 6 singlet pairings and 6 triplet pairings, as listed in Table I.

C. The pairing phase diagram

The doping x dependence of the largest pairing eigenvalues λ for various pairing symmetries is shown in Fig. 5(b). The parameter settings are $J_H = 0.1U$ and $U = 0.25$ eV, satisfying $U < U_c$, as shown in Fig. 4. The U dependence of λ is shown for $J_H = 0.1U$ in Fig. 6(a) and $J_H = 0.2U$ in Fig. 6(b) at $x = 0.6$. Eight out of the 12 possible pairing symmetries with relatively higher pairing eigenvalues are shown. Here we only consider the regime $x > 0.4$ because of the following two reasons. On the one hand, too low x might invalidate the rigid-band approximation as the band structure we adopt is for $x = 1$. On the other hand, the spin-glass phase instead of SC is experimentally detected for $x < 0.4$ [34,35], suggesting that the system should have already entered the spin-ordered phase in that doping regime, which invalidates the RPA treatment.

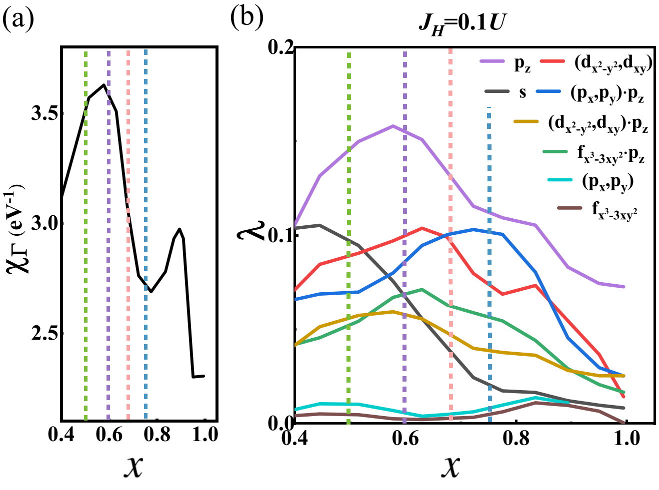

FIG. 5. (a) The hydrogen-doping level x dependence of the susceptibility $\chi(\mathbf{k})$ for the Γ point. (b) The largest pairing eigenvalues λ as a function of x for eight pairing symmetries with relatively higher λ under $U = 0.25$ eV, $J_H = 0.1U$. The dotted lines with different colors mark different x in $KH_xCr_3As_3$. Specifically, the green, purple, pink, and blue lines mark $x = 0.5$, $x = 0.6$, $x = 0.67$, and $x = 0.75$, respectively.

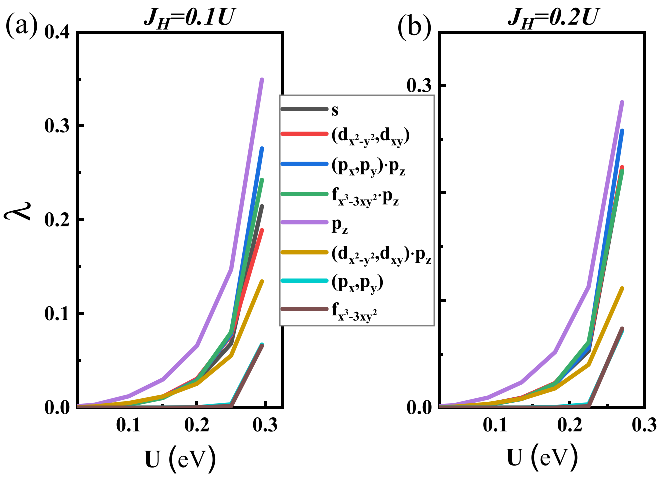

FIG. 6. Leading pairing eigenvalue λ as function of interaction U at $x = 0.6$ for (a) $J_H = 0.1U$ and (b) $J_H = 0.2U$. Only the eight strongest pairing-symmetry channels are shown.

Two important results are provided by Fig. 5(b). First, the triplet p_z-wave pairing is the leading pairing symmetry in the whole doping regime of $x \in (0.4, 1)$ relevant to experiments. This result suggests that the SC detected by experiments should be of p_z-wave pairing symmetry. Second, the doping dependence of the λ and hence the T_c of the obtained p_z-wave SC takes a domed shape peaking near the Lifshitz-transition point with $x \approx 0.6$. What is more, a comparison between Figs. 5(a) and 5(b) reveals the similarity between the $\lambda \sim x$ relation for the triplet p_z-wave SC and the $\chi_\Gamma \sim x$ relation. The physical reason for such similarity lies in that the ferromagnetic fluctuation reflected by χ_Γ favors the formation of triplet SC.

The distribution of the relative gap function of the obtained p_z-wave SC is shown on the α, β, γ, and δ FSs for the Lifshitz-transition doping level $x = 0.6$ in Figs. 7(a)–7(d). While the α, β, and γ FSs at this doping are 1D-like planes almost parallel to the (k_x, k_y) plane, the δ FSs take the shape of six bent tubes almost perpendicular to the (k_x, k_y) plane. Figures 7(a)–7(d) show that this gap function is sixfold rotation symmetric about the z axis, and changes sign upon reflection about the $k_z = 0$ plane, consistent with the p_z-wave pairing symmetry. Besides the aspect of symmetry, Figs. 7(a)–7(d) additionally show that the amplitude of the pairing gap on the δ FSs is lower than that on the other three FSs. This situation is more clear in Fig. 7(e) which shows the k_z dependence of the averaged gap function on the FSs with fixed k_z. The reason for this lies in that the $\mathbf{k}$ dependence of the gap function of the p_z-wave SC in the system can be approximated as $\Delta_{\mathbf{k}} \sim \Delta_0 \sin k_z$, which is small in the small-k_z regime $k_z \in (-1, 1)$ occupied by the δ FSs and large in the $k_z \in \pm(1.0, 1.6)$ regime occupied by the other three FSs. A similar situation is also verified for the doping level x slightly higher than the Lifshitz-transition point, with

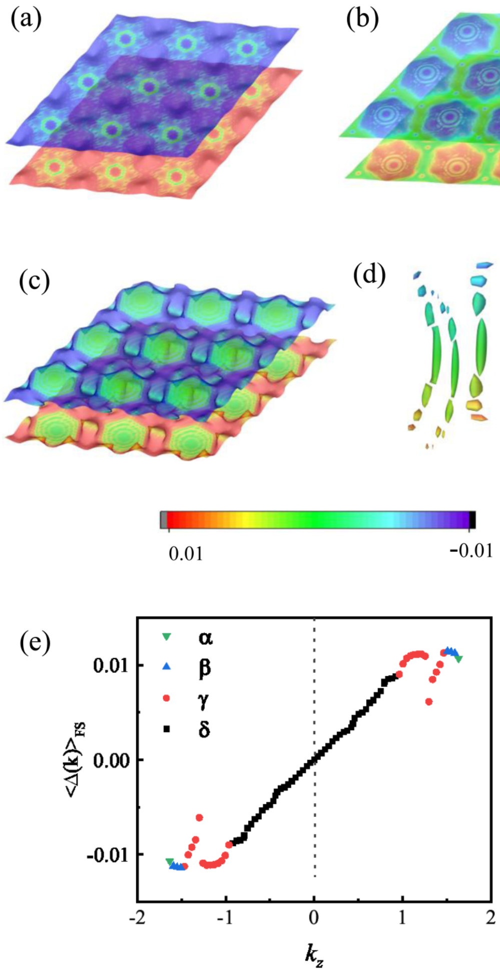

FIG. 7. (a) The pairing gap functions shown on different FSs for the p_z SC with $x = 0.6$. The FSs shown from (a) to (d) are α, β, γ, and δ, respectively. The three FSs have different k_z scales: for α FS, $k_z = \pm1.62$; for β FS, $k_z = \pm1.62$; for γ FS, $k_z = \pm1.45$; and for δ FS, $k_z = \pm0.8$. (e) The k_z dependence of the gap function averaged on the FS with fixed k_z.

only the tubelike δ FSs replaced by the 3D tubelike part of the γ FSs, with both occupying the small-k_z regime $k_z \in (-1, 1)$.

IV. LIFSHITZ TRANSITION ENHANCED p_z-WAVE SC

To understand the physical origin of the triplet p_z-wave pairing as well as the dome-shaped $\lambda \sim x$ relation curve peaking near the Lifshitz-transition point $x = 0.6$ as shown in Fig. 5(b), let us perform a more thorough investigation on the detailed band structure and the doping dependence of the FSs near the Lifshitz transition.

From Fig. 1(b), there is a gap between the γ and δ bands on the $k_z = 0$ plane slightly below the Fermi energy of $KHCr_3As_3$. The Fermi energy of the Lifshitz transition doping $x = 0.6$ is just located within this gap. To more clearly reflect the low-energy band structure near this Fermi energy, in Fig. 8(a) we choose a specified path on the $k_z = 0$ plane shown in the bottom inset, which shows that the γ and δ bands nearly cross each other, opening a tiny gap of about 1 meV shown in the upper inset, forming an approximate Dirac-Fermi point at $x = 0.6$. This approximate Dirac crossing suppresses the density of states (DOS) nearby, as verified by the dip in the total-DOS curve shown in Fig. 8(b). It is then a puzzle why the $T_c \sim x$ relation of the p_z-wave SC shown in Fig. 5(b) peaks near the Lifshitz-transition doping, as the suppressed DOS there is generally harmful for the formation of SC.

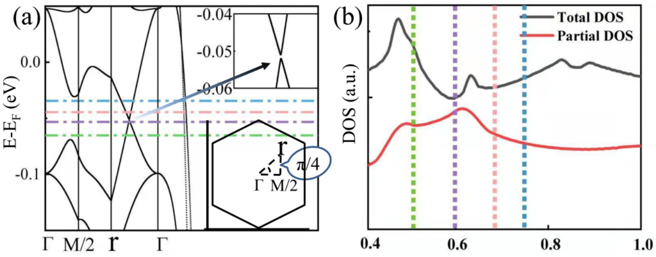

FIG. 8. (a) Band structure of KCr_3As_3H along the specified path as shown in the bottom inset where $|r_x| = |r_y| = |M/2|$. The enlarged approximate "Dirac cone" in the band structure is shown in the upper inset. (b) The doping x dependence of the total DOS (black) and the partial DOS (red) contributed by $k_z \in (1, 1.6)$ on the FSs. The dash-dotted lines in (a) and dotted lines in (b) with different colors mark different x, with the same convention as used in Fig. 5.

The solution of this puzzle lies in a known routine which governs the distribution of the pairing gap function on the FS of an *e*-*e* interaction-driven superconductor: the regimes with relatively large DOS on the FS should be distributed with relatively large pairing gap amplitudes, so that the system can gain more energy from the superconducting condensation [63]. Figure 8(a) and our following analysis for the doping dependence of the FSs both suggest that the Lifshitz transition mainly suppresses the DOS contributed by the small-$|k_z|$ regime $k_z \in (-1, 1)$. As Fig. 7 shows that the p_z-wave pairing amplitude is low in the regime $k_z \in (-1, 1)$, the Lifshitz transition is not harmful to the formation of SC with this pairing symmetry. More importantly, if we focus on the partial DOS contributed by the large-$|k_z|$ regime $k_z \in \pm(1.0, 1.6)$ on the FSs including the α and β FSs and the quasi-1D part of the γ FSs, this part of the DOS takes a peak near the Lifshitz-transition doping, as shown in Fig. 8(b). Such a maximized DOS in these k_z regimes on the FSs favors the formation of the p_z-wave pairing since its pairing amplitude, approximately proportional to $\sin k_z$, is large in these k_z regimes. Therefore, the partial-DOS peak shown in Fig. 8(b), in combination with the k_z dependence of the p_z-wave pairing gap function shown in Fig. 7, can well account for the domelike $T_c \sim x$ relation for the p_z-wave SC shown in Fig. 5(b).

Two further questions arise. Why is the partial DOS contributed by the large-$|k_z|$ regimes maximized near the Lifshitz transition? And why is the triplet p_z-wave pairing favored? The answer for the two questions lies in the presence of the type-II VHSs [48–52] in the band structure. To clarify this point, a thorough investigation on the evolution of the FSs with x is necessary. For this purpose, we choose four typical dopings $x = 0.75$, 0.67, 0.6, and 0.5 marked in Fig. 5 with their Fermi energies marked in Fig. 8(a), under which the p_z-wave pairing dominates other pairing symmetries. In the following, we study the 3D FSs and typical 2D cuts of the FSs in the fixed k_z planes for the four doping levels.

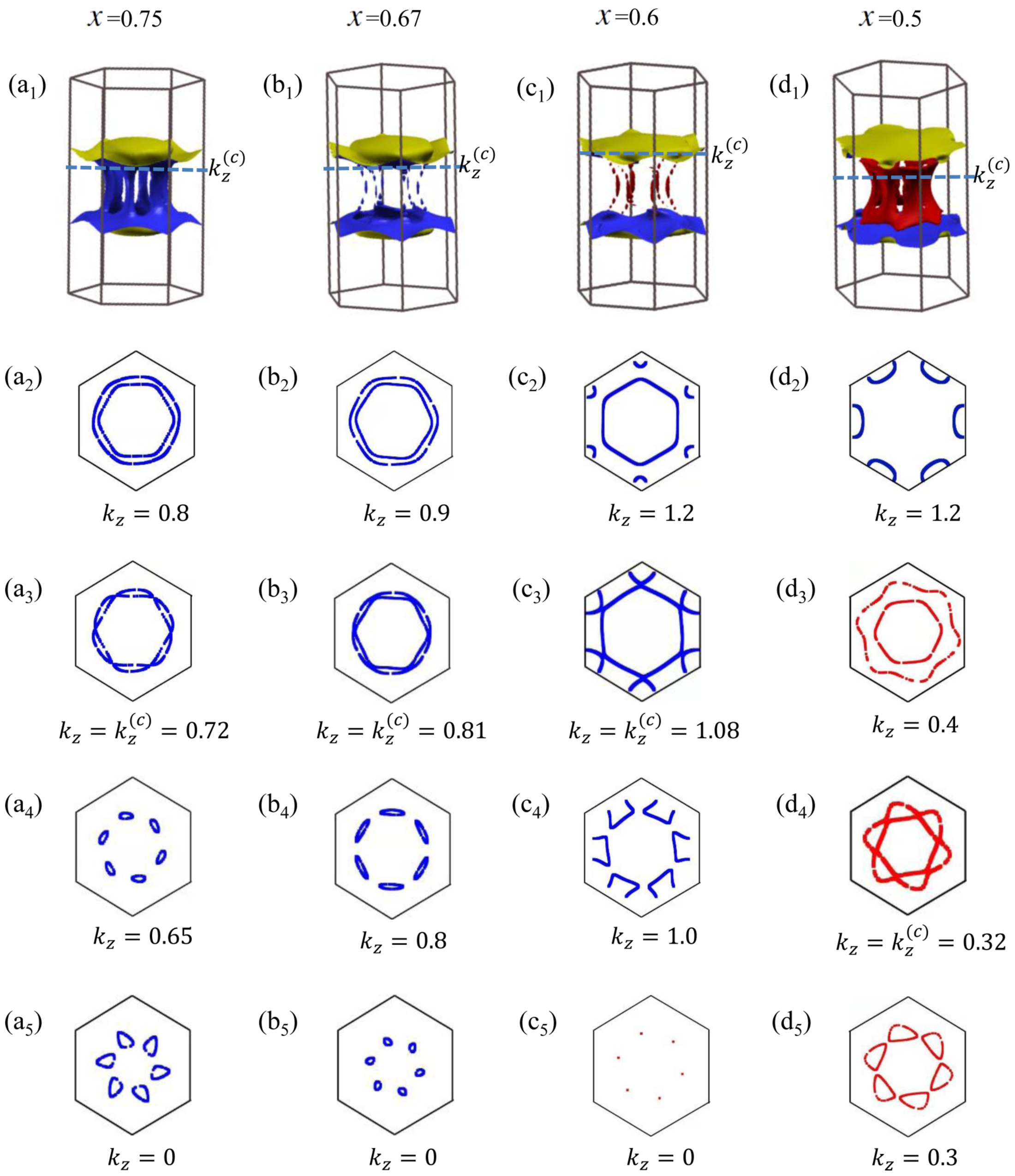

FIG. 9. 3D FSs and 2D cuts of the FSs on fixed k_z planes for $\mathrm{KCr_3As_3H}_x$ with typical doping levels (a_1–a_5) $x = 0.75$, (b_1–b_5) $x = 0.67$, (c_1–c_5) $x = 0.6$, and (d_1–d_5) $x = 0.5$ under the rigid-band approximation. For each x, the figure in the first row shows the 3D FSs and those in the remaining four rows show the 2D fixed-k_z cuts of the FSs with different k_z marked in each figure. Note that for each x, there exists a critical k_z marked as $k_z^{(c)}$: the 2D cuts of the FSs on the $k_z = \pm k_z^{(c)}$ plane are experiencing a 2D Lifshitz transition, forming the type-II VHSs [48–52]. The values of $k_z^{(c)}$ are marked in (a_3), (b_3), (c_3), and (d_4) for the four doping levels, respectively. The position of the $k_z = k_z^{(c)}$ plane is also marked in the 3D FSs for each doping. Blue denotes the γ FSs and red denotes the δ FSs.

We focus on the γ and δ FSs which will experience important variation with x, and ignore the α and β FSs.

For the doping level $x = 0.75$, the 3D FS is shown in Fig. 9(a_1), and the four typical 2D FS cuts are shown in Figs. 9(a_2)–9(a_5). For $x = 0.75$, the FS is only contributed from the γ band, and the δ FS is absent. Figure 9(a_1) shows that this FS is globally connected, consisting of two flat quasi-1D sheets nearly parallel with the (k_x, k_y) plane, connected by six bent tubelike FS sheets. The 3D FS cuts the $k_z = 0$ plane to form six symmetry-related pockets, as shown in Fig. 9(a_5). With increasing $|k_z|$, the size of the Fermi pockets in the fixed k_z cuts initially varies nonmonotonically, and finally increases monotonically until the adjacent pockets touch each other at the critical $k_z = \pm k_z^{(c)} = \pm 0.72$ to form a 2D Lifshitz transition, as shown in Fig. 9(a_3). The FS cuts on the $k_z = \pm k_z^{(c)}$ planes can be viewed as the boundary between the quasi-1D FS sheets and the tubelike FS sheets, as shown by the dashed line in Fig. 9(a_1). The FS cuts for $k_z = 0.8$ and $k_z = 0.65$ are shown in Figs. 9(a_2) and 9(a_4) for comparison. Obviously, the 2D Lifshitz transitions at $k_z = \pm k_z^{(c)}$ form the so-called type-II

VHS [48–52], in which the van Hove momenta are *not* located at time-reversal variant points. It was pointed out [48–52] that triplet SC would generally be favored near the type-II VHS, mediated by the ferromagnetic fluctuations brought about by the strong forward scatterings there. This explains the origin of the triplet SC in the system.

With decreasing x, the six tubelike FS sheets become thinner, until each of them is broken into several segments below $x \approx 0.7$, as shown in Fig. 9(b_1) for $x = 0.67$. Clearly, the size of the Fermi pockets on the $k_z = 0$ cut shown in Fig. 9(b_5) for $x = 0.67$ is smaller than that for $x = 0.75$. For $x = 0.67$, the six topmost and six bottommost tubelike FS sheets also grow thick enough at $k_z = \pm k_z^{(c)} = \pm 0.81$ so that any two adjacent tubes touch each other and consequently these tubes promptly evolve into the two flat quasi-1D FS sheets. The 2D FS cut at $k_z = k_z^{(c)} = 0.81$ shown in Fig. 9(b_3) again illustrates the type-II VHS, with the cases for $k_z = 0.8$ and 0.9 shown for comparison. Clearly, the $k_z^{(c)}$ is enhanced at this doping. Such enhancement of the $k_z^{(c)}$ favors the formation of the p_z-wave pairing because the divergence of the 2D DOS takes place at enhanced $|k_z|$ where the p_z-wave pairing gap amplitude is larger. This explains why the T_c for the p_z-wave SC is enhanced from $x = 0.75$ to $x = 0.67$.

When x further decreases to $x = 0.6$, all the inner broken segments of the six tubelike γ FS sheets vanish while the topmost and the bottommost segments still exist and are connected to the flat quasi-1D FS sheets, identifying the 3D-quasi-1D Lifshitz transition, as shown in Fig. 9(c_1). The residual topmost and bottommost segments are now more appropriately described as 12 thin antennas stuck out from the flat quasi-1D FS sheets. The $k_z^{(c)}$ now attains its maximum value $k_z^{(c)} = 1.08$ as shown in Fig. 9(c_3), and Figs. 9(c_2) and 9(c_4) for comparison, leading to the largest T_c for the p_z-wave pairing around $x = 0.6$. Meanwhile, another six separate tubelike δ FS sheets (red) appear, which cuts the $k_z = 0$ plane to form six very small pockets shown in Fig. 9(c_5). These six tubelike δ FSs grow thicker and thicker when x further decreases, and finally each two adjacent tubes touch each other again, as shown in Fig. 9(d_1) for $x = 0.5$. At $x = 0.5$, although the type-II VHSs are no longer present on any 2D fixed k_z cuts of the γ FSs, as shown in Fig. 9(d_2) for a typical $k_z = 1.2$, they appear on the 2D cuts of the δ FSs instead at $k_z = \pm k_z^{(c)} = \pm 0.32$, as shown in Fig. 9($d_4$), and Figs. 9($d_3$) and 9($d_5$) for comparison. Although these δ-band type-II VHSs also favor the triplet pairing, the T_c is lower than that of $x = 0.6$ as the $k_z^{(c)}$ is largely suppressed. Now we understand why the T_c for the p_z-wave SC is highest around the 3D-quasi-1D Lifshitz-transition doping $x = 0.6$.

To summarize this section, from detailed analysis on the hydrogen-doping x dependence of the 3D FSs and 2D cuts of the FSs in the fixed k_z planes, we have revealed the origin of the triplet p_z-wave SC as well as the dome-shaped $T_c \sim x$ relation peaking at the 3D-quasi-1D Lifshitz-transition doping. It turns out that the γ band contributes a special 3D FS which consists of two flat quasi-1D FS sheets connected by six tubelike FS sheets, the boundaries between the two parts located within two fixed k_z planes with $k_z = \pm k_z^{(c)}$. It is important that the type-II VHSs appear on these two boundaries, which favor the formation of triplet SC. What is more, the $k_z^{(c)}$ is largest near the 3D-quasi-1D Lifshitz-transition doping, which pushes the T_c of the triplet p_z-wave SC to its maximum because its $\Delta_{\mathbf{k}} \sim \Delta_0 \sin k_z$ gap form factor likes the VHSs with enhanced DOS locating at larger $|k_z|$.

V. DISCUSSION AND CONCLUSION

In conclusion, adopting the TB model constructed from the DFT band structure equipped with the extended Hubbard interactions, we use the RPA approach to study the pairing state of hydrogen-doped KCr_3As_3 under the rigid-band approximation. In the physically reasonable hydrogen-doping regime $x \in (0.4, 1)$ where evidence of SC has been experimentally identified, our RPA results yield the triplet p_z-wave pairing as the leading pairing symmetry. The $T_c \sim x$ relation for the p_z-wave SC takes a domed shape peaking at the 3D-quasi-1D Lifshitz-transition doping level. The physical origin of the triplet p_z-wave SC and its dome-shaped $T_c \sim x$ relation is related to the presence of the type-II VHSs [48–52] on the γ FS, owing to its special structure consisting of two flat quasi-1D FS sheets connected by six tubelike FS sheets, as summarized in the last paragraph in Sec. IV.

Note that the Lifshitz-transition doping level in our TB model is $x_c = 0.6$, which is slightly different from the $x_c = 0.73$ in our DFT band structure obtained via the QE code and the $x_c = 0.75$ in previous DFT band structure obtained via the VASP code [38], due to the deviation in the TB fitting. However, the detailed band structures and the shapes of the FSs for the three are similar near their Lifshitz-transition doping levels. Therefore, the $T_c \sim x$ relation for the realistic DFT band structures should take similar domed shapes peaking near the Lifshitz-transition dopings $x_c = 0.73$ or 0.75 [37], which are near the optimum doping $x_{\text{opt}} \in (0.65, 0.71)$ estimated from experiments [35]. Such a dome-shaped $T_c \sim x$ relation can serve as a mark to distinguish the *e-e* interaction-driven p_z-wave SC from the *s*-wave SC mediated by electron-phonon coupling, because if the pairing mechanism is the latter, the T_c should peak at the DOS maximum, while the Lifshitz transition just takes place at the doping level of the DOS minimum instead.

Here we have neglected the spin-orbit coupling (SOC) in the system as the SOC for the Cr 3*d* orbitals is weak. In the absence of SOC, the three spin components of the spin-triplet p_z-wave pairing are exactly degenerate. To lift up this degeneracy, a weak atomic SOC [21,47,64] adapting to the lattice symmetry can be added to the TB model. The resulting triplet-pairing component can be either $\uparrow\uparrow$, $\downarrow\downarrow$ with $S_z = \pm 1$ or $\uparrow\downarrow + \downarrow\uparrow$ with $S_z = 0$. If the latter is favored, the pairing state of the system would be a spin-U(1)-symmetry-protected topological SC similar with $K_2Cr_3As_3$ [64], hosting exactly flat surface bands on the (0, 0, 1) surface, which can serve as strong evidence for the p_z-wave SC.

ACKNOWLEDGMENT

We are grateful for the stimulating discussions with G.-H. Cao. This work is supported by the NSFC under Grants No. 12074031 and No. 11674025.

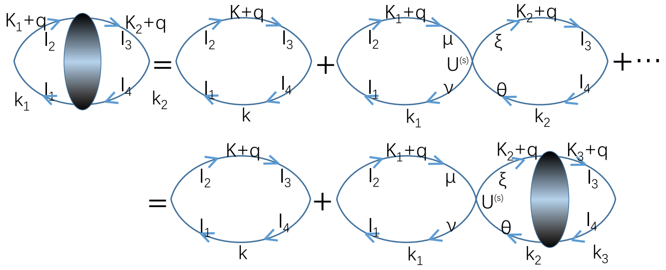

FIG. 10. Feynman's diagram for the renormalized susceptibilities in the RPA level.

APPENDIX A: THE MULTIORBITAL RPA APPROACH

The Hamiltonian adopted in our calculations is

$$H = H_{\mathrm{TB}} + H_{\mathrm{int}},$$

$$H_{\mathrm{int}} = U\sum_{i\mu} n_{i\mu\uparrow}n_{i\mu\downarrow} + V\sum_{i,\mu<\nu} n_{i\mu}n_{i\nu} + J_H\sum_{i,\mu<\nu}\left[\sum_{\sigma\sigma'} c^{+}_{i\mu\sigma}c^{+}_{i\nu\sigma'}c_{i\mu\sigma'}c_{i\nu\sigma} + \left(c^{+}_{i\mu\uparrow}c^{+}_{i\mu\downarrow}c_{i\nu\downarrow}c_{i\nu\uparrow} + \mathrm{H.c.}\right)\right]. \tag{A1}$$

Let us define the following bare susceptibility for the noninteracting case ($U = V = J_H = 0$),

$$\chi^{(0)l_1,l_2}_{l_3,l_4}(\mathbf{q},\tau) \equiv \frac{1}{N}\sum_{\mathbf{k_1},\mathbf{k_2}} \langle T_\tau c^{\dagger}_{l_1}(\mathbf{k_1},\tau)c_{l_2}(\mathbf{k_1}+\mathbf{q},\tau)c^{+}_{l_3}(\mathbf{k_2}+\mathbf{q},0)c_{l_4}(\mathbf{k_2},0)\rangle_0, \tag{A2}$$

where l_i ($i = 1,\dots,4$) denote orbital indices. The explicit formulism of $\chi^{(0)}$ in the momentum-frequency space is

$$\chi^{(0)l_1,l_2}_{l_3,l_4}(\mathbf{q},i\omega_n) = \frac{1}{N}\sum_{\mathbf{k},\alpha,\beta} \xi^{\alpha,*}_{l_1}(\mathbf{k})\xi^{\beta}_{l_2}(\mathbf{k}+\mathbf{q})\xi^{\beta,*}_{l_3}(\mathbf{k}+\mathbf{q})\xi^{\alpha}_{l_4}(\mathbf{k})\frac{n_F(\varepsilon^{\beta}_{\mathbf{k+q}}) - n_F(\varepsilon^{\alpha}_{\mathbf{k}})}{i\omega_n + \varepsilon^{\alpha}_{\mathbf{k}} - \varepsilon^{\beta}_{\mathbf{k+q}}}, \tag{A3}$$

where $\alpha/\beta = 1,\dots,6$ are band indices, $\varepsilon^{\alpha}_{\mathbf{k}}$ and $\xi^{\alpha}_{l}(\mathbf{k})$ are the αth eigenvalue and eigenvector of the $H_{TB}(\mathbf{k})$ matrix, respectively, and n_F is the Fermi-Dirac distribution function.

When the Hubbard interaction in Eq. (A1) is included, we can explicitly calculate the spin ($\chi^{(s)}$) and charge ($\chi^{(c)}$) susceptibilities as follows:

$$\chi^{(c)l_1,l_2}_{l_3,l_4}(\mathbf{q},\tau) \equiv \frac{1}{2N}\sum_{\mathbf{k_1},\mathbf{k_2},\sigma_1,\sigma_2} \langle T_\tau C^{\dagger}_{l_1,\sigma_1}(\mathbf{k_1},\tau)C_{l_2,\sigma_1}(\mathbf{k_1}+\mathbf{q},\tau)C^{+}_{l_3,\sigma_2}(\mathbf{k_2}+\mathbf{q},0)C_{l_4,\sigma_2}(\mathbf{k_2},0)\rangle,$$

$$\chi^{(s)l_1,l_2}_{l_3,l_4}(\mathbf{q},\tau) \equiv \frac{1}{2N}\sum_{\mathbf{k_1},\mathbf{k_2},\sigma_1,\sigma_2} \sigma_1\sigma_2\langle T_\tau C^{\dagger}_{l_1,\sigma_1}(\mathbf{k_1},\tau)C_{l_2,\sigma_1}(\mathbf{k_1}+\mathbf{q},\tau)C^{+}_{l_3,\sigma_2}(\mathbf{k_2}+\mathbf{q},0)C_{l_4,\sigma_2}(\mathbf{k_2},0)\rangle. \tag{A4}$$

Note that when $U = V = J_H = 0$ we have $\chi^{(c)} = \chi^{(s)} = \chi^{(0)}$. In the RPA level, the Cooper pair with momentum and orbital of $(\boldsymbol{k}l_3, -\boldsymbol{k}l_4)$ could be scattered into $(\boldsymbol{k'}l_1, -\boldsymbol{k'}l_2)$ by exchanging charge or spin fluctuations. This process can be explained graphically by Feynman diagrams shown as Fig. 10.

The renormalized spin and charge susceptibilities for the system are

$$\chi^{(s/c)}(\boldsymbol{k},i\omega_n) = [I \mp \chi^{(0)}(\boldsymbol{k},i\omega_n)U^{s/c}]^{-1}\chi^{(0)}(\boldsymbol{k},iw_n). \tag{A5}$$

where $\chi^{(s,c)}(\mathbf{k},i\omega_n)$, $\chi^{(0)}(\mathbf{k},i\omega_n)$, and $U^{(s,c)}$ are operated as 36×36 matrices (the upper or lower two indices are viewed as one number), and the nonzero elements $U^{(s/c)l_1l_2}_{l_3l_4}$ of $U^{s/c}$ are as follows:

$$U^{(s)l_1l_2}_{l_3l_4} = \begin{cases} U, & l_1 = l_2 = l_3 = l_4 \\ J_H, & l_1 = l_2 \neq l_3 = l_4 \\ J_H, & l_1 = l_3 \neq l_2 = l_4 \\ V, & l_1 = l_4 \neq l_3 = l_2, \end{cases} \tag{A6}$$

$$U^{(c)l_1l_2}_{l_3l_4} = \begin{cases} U, & l_1 = l_2 = l_3 = l_4 \\ 2V - J_H, & l_1 = l_2 \neq l_3 = l_4 \\ J_H, & l_1 = l_3 \neq l_2 = l_4 \\ 2J_H - V, & l_1 = l_4 \neq l_3 = l_2. \end{cases} \tag{A7}$$

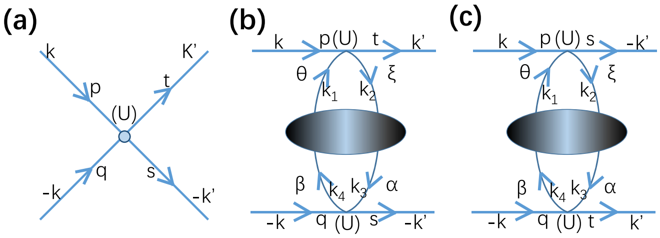

FIG. 11. Three processes which contribute the renormalized effective vertex considered in the RPA, with (a) the bare interaction vertex and (b), (c) the two second-order perturbation processes during which spin or charge fluctuations are exchanged between a Cooper pair.

For repulsive Hubbard interactions, the spin susceptibility is enhanced and the charge susceptibility is suppressed. Note that there is a critical interaction strength U_c which depends on the ratio J_H/U. Note that when the interaction strength U is higher than U_c, the denominator matrix $I - \chi^{(0)}(\boldsymbol{k}, i w_n)U^s$ in Eq. (A5) will have zero eigenvalues for some $\boldsymbol{q}$ and the renormalized spin susceptibility diverges there, which invalidates the RPA treatment. When $U < U_c$, the short-ranged spin or charge fluctuations would mediate Cooper pairing in the system.

Considering a Cooper pair with momentum and orbital $(\boldsymbol{k}'t, -\boldsymbol{k}'s)$; it could be scattered to $(\boldsymbol{k}p, -\boldsymbol{k}q)$ by exchanging charge or spin fluctuations. In the RPA level, The effective interaction induced by this process is as follows:

$$\mathrm{V}_{\mathrm{eff}}^{\mathrm{RPA}} = \frac{1}{\mathrm{N}} \sum_{pqst,\boldsymbol{k}\boldsymbol{k}'} \Gamma_{pq}^{st}(\boldsymbol{k}, \boldsymbol{k}') c_p^+(\boldsymbol{k}) c_q^+(-\boldsymbol{k}) c_s(-\boldsymbol{k}') c_t(\boldsymbol{k}'). \tag{A8}$$

We consider the three processes in Fig. 11 [65] which contribute to the effective vertex $\Gamma_{st}^{pq}(\boldsymbol{k}, \boldsymbol{k}')$, where Fig. 11(a) shows the bare interaction vertex and Figs. 11(b) and 11(c) represent the two second-order perturbation processes during which spin or charge fluctuations are exchanged between a Cooper pair. Hence this effective interaction process can be divided by spin pairings into singlet channel and triplet channel.

In the singlet channel, the effective vertex $\Gamma_{st}^{pq}(k, k')$ is given as follows:

$$\begin{aligned}\Gamma_{st}^{pq(s)}(k, k') = {}& \left(\frac{U^{(c)} + 3U^{(s)}}{4}\right)_{qs}^{pt} + \frac{1}{4}[3U^{(s)}\chi^{(s)}(k - k')U^{(s)} - U^{(c)}\chi^{(c)}(k - k')U^{(c)}]_{qs}^{pt} \\ & + \frac{1}{4}[3U^{(s)}\chi^{(s)}(k + k')U^{(s)} - U^{(c)}\chi^{(c)}(k + k')U^{(c)}]_{qt}^{ps},\end{aligned} \tag{A9}$$

while in the triplet channel, it is

$$\begin{aligned}\Gamma_{st}^{pq(t)}(k, k') = {}& \left(\frac{U^{(c)} - U^{(s)}}{4}\right)_{qs}^{pt} - \frac{1}{4}[U^{(s)}\chi^{(s)}(k - k')U^{(s)} + U^{(c)}\chi^{(c)}(k - k')U^{(c)}]_{qs}^{pt} \\ & + \frac{1}{4}[U^{(s)}\chi^{(s)}(k + k')U^{(s)} + U^{(c)}\chi^{(c)}(k + k')U^{(c)}]_{qt}^{ps}.\end{aligned} \tag{A10}$$

Notice that the vertex $\Gamma_{st}^{pq}(k, k')$ has been symmetrized for the singlet case and antisymmetrized for the triplet case. Generally we neglect the frequency dependence of Γ and replace it by $\Gamma_{st}^{pq}(k, k') \approx \Gamma_{st}^{pq}(\mathbf{k}, \mathbf{k}', 0)$.

Considering only intraband pairings, we obtain the following effective pairing interaction on the FS:

$$V_{\mathrm{eff}} = \frac{1}{N} \sum_{\alpha\beta,\mathbf{k}\mathbf{k}'} V^{\alpha\beta}(\mathbf{k}, \mathbf{k}') c_\alpha^\dagger(\mathbf{k}) c_\alpha^\dagger(-\mathbf{k}) c_\beta(-\mathbf{k}') c_\beta(\mathbf{k}'), \tag{A11}$$

where $\alpha/\beta = 1, \dots, 6$ are band indices. From the effective pairing interaction (A11), one can obtain the following linearized gap equation [21,41,42] to determine the T_c and the leading pairing symmetry of the system:

$$-\frac{1}{(2\pi)^3} \sum_\beta {}_{FS} d^2\mathbf{k}'_\parallel \frac{V^{\alpha\beta}(\mathbf{k}, \mathbf{k}')}{v_F^\beta(\mathbf{k}')} \Delta_\beta(\mathbf{k}') = \lambda \Delta_\alpha(\mathbf{k}). \tag{A12}$$

This equation can be looked upon as an eigenvalue problem, where the normalized eigenvector $\Delta_\alpha(\mathbf{k})$ represents the relative gap function on the αth FS patches near T_c, and eigenvalue λ is related to T_c through $T_c \propto e^{-1/\lambda}$. The leading pairing symmetry is determined by the largest eigenvalue λ of Eq. (A12).

[1] J.-K. Bao, J.-Y. Liu, C.-W. Ma, Z.-H. Meng, Z.-T. Tang, Y.-L. Sun, H.-F. Zhai, H. Jiang, H. Bai, C.-M. Feng, Z.-A. Xu, and G.-H. Cao, Superconductivity in Quasi-One-Dimensional $\mathrm{K_2Cr_3As_3}$ with Significant Electron Correlations, Phys. Rev. X **5**, 011013 (2015).

[2] Z.-T. Tang, J.-K. Bao, Y. Liu, Y.-L. Sun, A. Ablimit, H.-F. Zhai, H. Jiang, C.-M. Feng, Z.-A. Xu, and G.-H. Cao, Unconventional superconductivity in quasi-one-dimensional $\mathrm{Rb_2Cr_3As_3}$, Phys. Rev. B **91**, 020506(R) (2015).

[3] Z.-T. Tang, J.-K. Bao, Z. Wang, H. Bai, H. Jiang, Y. Liu, H.-F. Zhai, C.-M. Feng, Z.-A. Xu, and G.-H. Cao, Superconductivity in quasi-one-dimensional $\mathrm{Cs_2Cr_3As_3}$ with large interchain distance, Sci. China Mater. **58**, 16 (2015).

[4] G.-M. Pang, M. Smidman, W.-B. Jiang, J.-K. Bao, Z.-F. Weng, Y.-F. Wang, L. Jiao, J.-L. Zhang, G.-H. Cao, and H.-Q. Yuan, Evidence for nodal superconductivity in quasi-one-dimensional $\mathrm{K_2Cr_3As_3}$, Phys. Rev. B **91**, 220502(R) (2015).

[5] H.-Z. Zhi, T. Imai, F.-L. Ning, J.-K. Bao, and G.-H. Cao, NMR Investigation of the Quasi-One-Dimensional Superconductor $\mathrm{K_2Cr_3As_3}$, Phys. Rev. Lett. **114**, 147004 (2015).

[6] D.-T. Adroja, A. Bhattacharyya, M. Telling, Y. Feng, M. Smidman, B. Pan, J. Zhao, A. D. Hillier, F. L. Pratt, and A. M. Strydom, Superconducting ground state of quasi-one-dimensional $\mathrm{K_2Cr_3As_3}$ investigated using μSR measurements, Phys. Rev. B **92**, 134505 (2015).

[7] T. Kong, S. L. Bud'ko, and P. C. Canfield, Anisotropic H_{c2} thermodynamic and transport measurements, and pressure dependence of T_c in $\mathrm{K_2Cr_3As_3}$ single crystals, Phys. Rev. B **91**, 020507(R) (2015).

[8] J. Yang, Z.-T. Tang, G.-H. Cao, and G.-Q. Zheng, Ferromagnetic Spin Fluctuation and Unconventional Superconductivity in $\mathrm{Rb_2Cr_3As_3}$ Revealed by ^{75}As NMR and NQR, Phys. Rev. Lett. **115**, 147002 (2015).

[9] F. F. Balakirev, T. Kong, M. Jaime, R. D. McDonald, C. H. Mielke, A. Gurevich, P. C. Canfield, and S. L. Bud'ko, Anisotropy reversal of the upper critical field at low temperatures and spin-locked superconductivity in $\mathrm{K_2Cr_3As_3}$, Phys. Rev. B **91**, 220505(R) (2015).

[10] X. F. Wang, C. Roncaioli, C. Eckberg, H. Kim, J. Yong, Y. Nakajima, S. R. Saha, P. Y. Zavalij, and J. Paglione, Tunable electronic anisotropy in single-crystal $A_2\mathrm{Cr_3As_3}$ (A = K, Rb) quasi-one-dimensional superconductors, Phys. Rev. B **92**, 020508(R) (2015).

[11] G. Pang, M. Smidman, W. Jiang, Y. Shi, J. Bao, Z. Tang, Z. Weng, Y. Wang, L. Jiao, and J. Zhang, Penetration depth measurements of $\mathrm{K_2Cr_3As_3}$ and $\mathrm{Rb_2Cr_3As_3}$, J. Magn. Magn. Mater. **400**, 84 (2016).

[12] G.-H. Cao, J.-K. Bao, Z.-T. Tang, Y. Liu, and H. Jiang, Peculiar properties of $\mathrm{Cr_3As_3}$-chain-based superconductors, Philos. Mag. **97**, 591 (2017).

[13] D. T. Adroja, A. Bhattacharyya, M. Smidman, A. D. Hillier, Y. Feng, B. Pan, J. Zhao, M. R. Lees, A. M. Strydom, and P. K. Biswas, Nodal superconducting gap structure in the quasi-one-dimensional $\mathrm{Cs_2Cr_3As_3}$ investigated using μSR measurements, J. Phys. Soc. Jpn. **86**, 044710 (2017).

[14] K.-M. Taddei, Q. Zheng, A.-S. Sefat, and C. Cruz, Coupling of structure to magnetic and superconducting orders in quasi-one-dimensional $\mathrm{K_2Cr_3As_3}$, Phys. Rev. B **96**, 180506(R) (2017).

[15] K. Zhao, Q.-G. Mu, T. Liu, B.-J. Pan, B.-B. Ruan, L. Shan, G.-F. Chen, and Z.-A. Ren, Superconductivity in novel quasi-one-dimensional ternary molybdenum pnictides $\mathrm{Rb_2Mo_3As_3}$ and $\mathrm{Cs_2Mo_3As_3}$, arXiv:1805.11577.

[16] Q.-G. Mu, B.-B. Ruan, B.-J. Pan, T. Liu, J. Yu, K. Zhao, G.-F. Chen, and Z.-A. Ren, Ion-exchange synthesis and superconductivity at 8.6 K of $\mathrm{Na_2Cr_3As_3}$ with quasi-one-dimensional crystal structure, Phys. Rev. Materials **2**, 034803 (2018).

[17] Q.-G. Mu, B.-B. Ruan, K. Zhao, B.-J. Pan, T. Liu, L. Shan, G.-F. Chen, and Z.-A. Ren, Superconductivity at 10.4 K in a novel quasi-one-dimensional ternary molybdenum pnictide $\mathrm{K_2Mo_3As_3}$, Sci. Bull. **63**, 952 (2018).

[18] J. Luo, J. Yang, R. Zhou, Q.-G. Mu, T. Liu, Z.-A. Ren, C.-J. Yi, Y.-G. Shi, and G.-Q. Zheng, Tuning the Distance to a Possible Ferromagnetic Quantum Critical Point in $A_2\mathrm{Cr_3As_3}$, Phys. Rev. Lett. **123**, 047001 (2019).

[19] H. Jiang, G.-H. Cao, and C. Cao, Electronic structure of quasi-one-dimensional superconductor $\mathrm{K_2Cr_3As_3}$ from first-principles calculations, Sci. Rep. **5**, 16054 (2015).

[20] X. Wu, C. Le, J. Yuan, H. Fan, and J. Hu, Magnetism in quasi-one-dimensional $A_2\mathrm{Cr_3As_3}$ (A = K, Rb) superconductors, Chin. Phys. Lett. **32**, 057401 (2015).

[21] X.-X. Wu, F. Yang, C.-C. Le, H. Fan, and J.-P. Hu, Triplet p_z-wave pairing in quasi-one-dimensional $A_2\mathrm{Cr_3As_3}$ auperconductors (A = K, Rb, Cs), Phys. Rev. B **92**, 104511 (2015).

[22] L.-D. Zhang, X.-X. Wu, H. Fan, F. Yang, and J.-P. Hu, Revisitation of superconductivity in $\mathrm{K_2Cr_3As_3}$ based on the six-band model, Europhys. Lett. **113**, 37003 (2016).

[23] Y. Zhou, C. Cao, and F.-C. Zhang, Theory for superconductivity in alkali chromium arsenides $A_2\mathrm{Cr_3As_3}$ (A = K, Rb, Cs), Sci. Bull. **62**, 208 (2017).

[24] J.-J. Miao, F.-C. Zhang, and Y. Zhou, Instability of three-band Tomonaga-Luttinger liquid: Renormalization group analysis and possible application to $\mathrm{K_2Cr_3As_3}$, Phys. Rev. B **94**, 205129 (2016).

[25] H. Zhong, X.-Y. Feng, H. Chen, and J. Dai, Formation of Molecular-Orbital Bands in a Twisted Hubbard Tube: Implications for Unconventional Superconductivity in $\mathrm{K_2Cr_3As_3}$, Phys. Rev. Lett. **115**, 227001 (2015).

[26] X. Wu, F. Yang, S. Qin, H. Fan, and J. Hu, Experimental consequences of p_z-wave spin triplet superconductivity in $\mathrm{A_2Cr_3As_3}$, arXiv:1507.07451.

[27] R.-Y. Chen and N.-L. Wang, Progress in Cr- and Mn-based superconductors: A key issues review, Rep. Prog. Phys. **82**, 012503 (2019).

[28] J. Yang, J. Luo, C.-J. Yi, Y.-G. Shi, Y. Zhou, and G.-Q. Zheng, Spin-triplet superconductivity in $\mathrm{K_2Cr_3As_3}$, Sci. Adv. **7**, eabl4432 (2021).

[29] J.-K. Bao, L. Li, Z.-T. Tang, Y. Liu, Y.-K. Li, H. Bai, C.-M. Feng, Z.-A. Xu, and G.-H. Cao, Cluster spin-glass ground state in quasi-one-dimensional $\mathrm{KCr_3As_3}$, Phys. Rev. B **91**, 180404(R) (2015).

[30] Z.-T. Tang, J.-K. Bao, Y. Liu, H. Bai, H. Jiang, H.-F. Zhai, C.-M. Feng, Z.-A. Xu, and G.-H. Cao, Synthesis, crystal structure and physical properties of quasi-one-dimensional $\mathrm{ACr_3As_3}$ (A = Rb, Cs), Sci. China Mater. **58**, 543 (2015).

[31] Q.-G. Mu, B.-B. Ruan, B.-J. Pan, T. Liu, J. Yu, K. Zhao, G.-F. Chen, and Z.-A. Ren, Superconductivity at 5 K in quasi-one dimensional Cr-based $\mathrm{KCr_3As_3}$ single crystals, Phys. Rev. B **96**, 140504(R) (2017).

[32] T. Liu, Q.-G. Mu, B.-J. Pan, J. Yu, B.-B. Ruan, K. Zhao, G.-F. Chen, and Z.-A. Ren, Superconductivity at 7.3 K in the

133-type Cr-based $RbCr_3As_3$ single crystals, Europhys. Lett. **120**, 27006 (2017)

[33] C. Cao, H. Jiang, X.-Y. Feng, and J. Dai, Reduced dimensionality and magnetic frustration in KCr_3As_3, Phys. Rev. B **92**, 235107 (2015).

[34] Y. Feng, X. Zhang, Y. Hao, A. D. Hillier, D. T. Adroja, and J. Zhao, Magnetic ground state of KCr_3As_3, Phys. Rev. B **99**, 174401 (2019).

[35] K. M. Taddei, L. D. Sanjeewa, B.-H. Lei, Y. H. Fu, Q. Zheng, D. J. Singh, A. S. Sefat, and C. dela Cruz, Tuning from frustrated magnetism to superconductivity in quasi-one-dimensional KCr_3As_3 through hydrogen doping, Phys. Rev. B **100**, 220503(R) (2019).

[36] J.-J. Xiang, Y.-L. Yu, S.-Q. Wu, B.-Z. Li, Y.-T. Shao, Z.-T. Tang, J.-K. Bao, and G.-H. Cao, Superconductivity induced by aging and annealing in $K_{1-\delta}Cr_3As_3H_x$, Phys. Rev. Materials **3**, 114802 (2019).

[37] J.-J. Xiang, Y.-T. Shao, Y.-W. Cui, L.-P. Nie, S.-Q. Wu, B.-Z. Li, Z. Ren, T. Wu, and G.-H. Cao, Superconductivity and phase separation in electrochemically hydrogenized $K_{1-\delta}Cr_3As_3H_x$, Phys. Rev. Materials **4**, 124802 (2020).

[38] S.-Q. Wu, C. Cao, and G.-H. Cao, Lifshitz transition and nontrivial H-doping effect in the Cr-based superconductor $KCr_3As_3H_x$, Phys. Rev. B **100**, 155108 (2019).

[39] K. Kubo, Pairing symmetry in a two-orbital Hubbard model on a square lattice, Phys. Rev. B **75**, 224509 (2007).

[40] K. Kuroki, S. Onari, R. Arita, H. Usui, Y. Tanaka, H. Kontani, and H. Aoki, Unconventional Pairing Originating from the Disconnected Fermi Surfaces of Superconducting $LaFeAsO_{1-x}F_x$, Phys. Rev. Lett. **101**, 087004 (2008).

[41] S. Graser, T. A. Maier, P. J. Hirschfeld, and D. J. Scalapino, Near-degeneracy of several pairing channels in multiorbital models for the Fe pnictides, New J. Phys. **11**, 025016 (2009).

[42] T. A. Maier, S. Graser, P. J. Hirschfeld, and D. J. Scalapino, d-wave pairing from spin fluctuations in the $K_xFe_{2-y}Se_2$ superconductors, Phys. Rev. B **83**, 100515(R) (2011).

[43] F. Liu, C.-C. Liu, K. Wu, F. Yang, and Y. Yao, $d + id'$ Chiral Superconductivity in Bilayer Silicene, Phys. Rev. Lett. **111**, 066804 (2013).

[44] C.-C. Liu, L.-D. Zhang, W.-Q. Chen, and F. Yang, Chiral SDW and $d + id$ Superconductivity in the Magic-Angle-Twisted Bilayer Graphene, Phys. Rev. Lett. **121**, 217001 (2018).

[45] T. Takimoto, T. Hotta, and K. Ueda, Strong-coupling theory of superconductivity in a degenerate Hubbard model, Phys. Rev. B **69**, 104504 (2004).

[46] K. Yada and H. Kontani, Origin of the weak pseudo-gap behaviors in $Na_{0.35}CoO_2$: Absence of small hole pockets, J. Phys. Soc. Jpn. **74**, 2161 (2005).

[47] L.-D. Zhang, X.-M. Zhang, J.-J. Hao, W. Huang, and F. Yang, Singlet $s^{\pm}$-wave pairing in quasi-one-dimensional ACr_3As_3 (A = K, Rb, Cs) superconductors, Phys. Rev. B **99**, 094511 (2019).

[48] H. Yao and F. Yang, Topological odd-parity superconductivity at type-II two-dimensional van Hove singularities, Phys. Rev. B **92**, 035132 (2015).

[49] T.-X. Ma, F. Yang, H. Yao, and H.-Q. Lin, Possible triplet $p + ip$ superconductivity in graphene at low filling, Phys. Rev. B **90**, 245114 (2014).

[50] Zi Yang Meng, F. Yang, K.-S. Chen, H. Yao, and H.-Y. Kee, Evidence for spin-triplet odd-parity superconductivity close to type-II van Hove singularities, Phys. Rev. B **91**, 184509 (2015).

[51] X. Chen, Y.-G. Yao, H. Yao, F. Yang, and J. Ni, Topological $p + ip$ superconductivity in doped graphene-like single-sheet materials BC_3, Phys. Rev. B **92**, 174503 (2015).

[52] L.-D. Zhang, F. Yang, and Y.-G. Yao, Itinerant ferromagnetism and $p + ip$ superconductivity in doped bilayer silicene, Phys. Rev. B **92**, 104504 (2015).

[53] P. Giannozzi, Jr., O. Andreussi, T. Brumme, O. Bunau, M.-B. Nardelli, M. Calandra, R. Car, C. Cavazzoni, D. Ceresoli, M. Cococcioni, N. Colonna, I. Carnimeo, A.-D. Corso, S.-de Gironcoli, P. Delugas, R. A. DiStasio, Jr., A. Ferretti, A. Floris, G. Fratesi, G. Fugallo *et al.*, Advanced capabilities for materials modelling with QUANTUM ESPRESSO, J. Phys.: Condens. Matter **29**, 465901 (2017).

[54] J. P. Perdew, K. Burke, and M. Ernzerhof, Generalized Gradient Approximation Made Simple, Phys. Rev. Lett. **77**, 3865 (1996).

[55] A. Mostofi, J. Yates, G. Pizzi, Y. Lee, I. Souza, D. Vanderbilt, and N. Marzari, An updated version of WANNIER90: A tool for obtaining maximally-localised Wannier functions, Comput. Phys. Commun. **185**, 2309 (2014).

[56] I. Mazin, Electronic structure and magnetism in the frustrated antiferromagnet $LiCrO_2$: First-principles calculations, Phys. Rev. B **75**, 094407 (2007).

[57] J.-J. Hao, M. Zhang, X. Wu, and F. Yang, Topological p_z-wave nodal-line superconductivity with flat surface bands in the $AH_xCr_3As_3$ (A = Na, K, Rb, Cs) superconductors, arXiv:2201.10089.

[58] See Supplemental Material at http://link.aps.org/supplemental/10.1103/PhysRevB.105.134509 for the tight-binding parameters appearing in Eq. (2).

[59] S. Raghu, A. Kivelson, and D. J. Scalapino, Superconductivity in the repulsive Hubbard model: An asymptotically exact weak-coupling solution, Phys. Rev. B **81**, 224505 (2010).

[60] D. J. Scalapino, A common thread: The pairing interaction for unconventional superconductors, Rev. Mod. Phys. **84**, 1383 (2012).

[61] W. Kohn and J. M. Luttinger, New Mechanism for Superconductivity, Phys. Rev. Lett. **15**, 524 (1965).

[62] W. Cho, R. Thomale, S. Raghu, and S. A. Kivelson, Band structure effects on the superconductivity in Hubbard models, Phys. Rev. B **88**, 064505 (2013).

[63] J. Hu and H. Ding, Local antiferromagnetic exchange and collaborative Fermi surface as key ingredients of high temperature superconductors, Sci. Rep. **2**, 381 (2012)

[64] C.-C. Liu, C. Lu, L.-D. Zhang, X.-X. Wu, C. Fang, and F. Yang, Intrinsic topological superconductivity with exactly flat surface bands in the quasi-one-dimensional $A_2Cr_3As_3$ (A = Na, K, Rb, Cs) superconductors, Phys. Rev. Research **2**, 033050 (2020).

[65] M. Zhang, Y. Zhang, H.-M. Guo, and F. Yang, Theory of unconventional superconductivity in nickelate-based materials, Chin. Phys. B **30**, 108204 (2021).